═══ *Optoelectronics and optoelectronic devices* ═══

Influence of perovskite thickness on the performance of silver-doped NaZnBr$_3$ perovskite solar cells using SCAPS software

M.O. Abdulmalik[1,3,*], E. Danladi[2]

[1]*Department of Physics, Confluence University of Science and Technology, Osara, Kogi State, Nigeria*
[2]*Department of Physics, Federal University of Health Sciences, Otukpo, Benue State, Nigeria*
[3]*Department of Physics, University of Nairobi, Nairobi, Kenya*
[*]*Corresponding author e-mail: abdulmalikmo@custech.edu.ng*

Abstract. The absorbing layer thickness is a crucial parameter that significantly impacts the performance of perovskite solar cells (PSCs). In this study, we investigated the influence of the thickness of absorbing layer on the performance of silver-doped NaZnBr$_3$ perovskite solar cells using the one-dimensional solar cell capacitance simulator (SCAPS-1D) software. The absorbing layer thickness was varied in the range of 0.1 to 1.3 μm. The initial solar cell after simulation gave an open-circuit voltage (V_{oc}) of 1.174 V, short circuit current density (J_{sc}) of 14.012 mA/cm^2, fill factor (FF) of 79.649%, and the power conversion efficiency (PCE) of 13.101%. For the optimized thickness of the perovskite layer of 1.0 μm, the following solar cell characteristics were obtained: $V_{oc} = 1.197$ V, $J_{sc} = 18.184$ mA·cm^{-2}, FF = 79.110%, and PCE = 17.215%. A 31% and 30% increase of the PCE and J_{sc}, respectively, was observed for the optimized device parameters as compared to the initial ones. Such finding confirms the premise for excellent photon management and enhancement of PSCs performance by selecting the thickness of absorbing layer.

Keywords: SCAPS 1-D, perovskite solar cells, absorbing layer, current density, power conversion efficiency.

1. Introduction

Perovskite solar cells (PSCs) absorbing layers exhibit excellent properties such as high optical absorption capacity [1], easy synthesis route, high power conversion efficiency (PCE), low exciton binding energy, and long electron and hole diffusion lengths [2, 3]. Due to these advantages, PSCs attract great research interest in the photovoltaic (PV) sector. PCE of PSCs as high as 25.5% has been reported by some studies [4], indicating the prospects of PSCs and making them comparable to silicon-based solar cells.

In PSCs, the perovskite material plays a significant role in photon absorption, photogeneration of charge carriers and injecting them into the device structure. The chemical structure of hybrid perovskites is AMX$_3$, where A is an organic cation (methylammonium or formamidinium), M is a metal, and X is a halide atom. Perovskite materials are ambipolar in nature, which allows them to conduct both electrons and holes simultaneously [5]. The photogenerated electrons and holes are collected by an electron transport material (ETM) and a hole transport material (HTM), respectively [6].

The best performance is demonstrated by PSCs made of lead-based perovskites of inorganic-organic hybrids. In 2018, the efficiency of 25.2% for a perovskite/silicon tandem cell was achieved by Sahli *et al*. [7]. However, lead-based PSCs are unstable and toxic. Due to the toxic nature of lead, use of lead-based materials that can be ingested or absorbed by humans has been banned. Large-scale production of unstable lead-based PSCs can induce health disasters, negative impacts on the environment and ecosystems and threaten both human and non-human lives [8]. Hence, it is paramount to find materials with comparable or superior properties compared with lead, which are at the same time non-toxic and not prone to degradation in order to achieve clean energy systems. Over recent years, research has been geared towards lead-free perovskites with much emphasis on inorganic derivatives [9].

In PSCs, titania (TiO$_2$) is the most commonly used electron transport material. However, its flexibility for commercialization is limited by its deposition technique, which requires high temperatures [10].

Zinc oxide (ZnO) has attracted attention as an alternative to TiO$_2$ ETM for PSCs due to its unique

properties such as stability against photocorrosion, large exciton binding energy (60 eV), high electron mobility of 115 to 155 cm$^2 \cdot$V$^{-2} \cdot$s^{-2}, and the same value of the bandgap as that of TiO$_2$.

Aluminium (Al) impurity [11, 12] can be used to extrinsically dope ZnO in order to improve its electrical conductivity. The ionic radius of Al^{3+} (0.54 Å) is smaller than that of Zn^{2+} (0.74 Å). Therefore, a small amount of Al^{3+} substitutes Zn^{2+} in the lattice sites acting as a dopant and enhancing the conductivity of ZnO as ETM at the same time maintaining its excellent transparency in the visible light region [12]. Undoped ZnO as ETM in PSCs induces a relatively low PCE due to the reaction of organic cations (CH$_3$NH$_3$$^+$) of the perovskite material with the ZnO ETM, which does not take place in the Al doped ZnO ETM [13].

The PSC performance greatly depends on the thickness of the absorbing layer as photoinduced charge carriers are generated there. The diffusion length of charge carriers is affected as the thickness of the absorbing layer has direct influence on the photovoltaic performance of the device. For too thick absorbing layers, the series resistance increases and the charge carriers have a high probability of recombining upon drifting to the charge transport layers. However, too thin absorbing layers will have poor photon absorption, which will lead to low photocurrent values and reduction in the overall device performance [14].

The charge collection efficiency, series resistance, fill factor, and generally PCE of PSCs depend on the perovskite layer thickness [15, 16]. Therefore, the appropriate thickness of the perovskite absorbing layer in PSCs devices should be determined.

In this study, the influence of the thickness of absorbing layer on the photovoltaic parameters such as power conversion efficiency, fill factor (FF), short circuit current density (J_{sc}), and open-circuit voltage (V_{oc}) were investigated using the SCAPS-1D software. The following device configuration was considered: glass/fluorine doped tin oxide (FTO)/aluminium doped zinc oxide (ZnO:Al)/sodium-zinc-tribromide (NaZnBr$_3$)/ copper iodide (CuI)/gold (Ag). The simulations were done by varying the absorbing layer thickness from 0.1 to 1.3 μm, while other device parameters presented in Tables 1 and 2 remained constant.

2. Device modeling and simulation methods

2.1. Simulation methodology

As mentioned above, the latest-version of SCAPS-1D software (3.3.10, developed by Prof. Marc Burgelman and his co-workers from the Ghent University, Belgium) was used for the study. This software was earlier used for numerical simulations of similar PV devices [17–19]. It implements standard numerical methods to solve the differential equations, which model photovoltaic response of any solar cell, similar to many other simulation softwares. The equations can be classified as follows:

(i) Poisson equation

This equation describes the behaviour of the electrical potential φ as a function of the distribution of various types of electrical charges inside the solar cell. In the equation, q is the electric charge, ε_0 is the absolute dielectric constant, ε_r are the relative dielectric constants of each material layer, N_D/N_A is the donor/acceptor dopant concentration, ρ_p/ρ_n is the hole/electron charge density, and $p(x)/n(x)$ is the hole/electron concentration as a function of the thickness x, respectively. The Poisson equation is thus defined as follows:

$$\frac{d^2\varphi(x)}{dx^2} = \frac{q}{\varepsilon_0\varepsilon_r}\left(p(x) - n(x) + N_D - N_A + \rho_p - \rho_n\right). \qquad (1)$$

(ii) Continuity equations

These equations establish the relations between the gradients of electron (J_n) and hole current density (J_p) and position-dependent generation (G) and recombination rate (R) of charge carriers. They can be written as follows:

$$\frac{dJ_n}{dx} = G - R, \qquad (2)$$

$$\frac{dJ_p}{dx} = G - R. \qquad (3)$$

(iii) Charge transport equations

A PV cell is intrinsically a diode in nature. Therefore, the diode charge transport equations may be applied to it. These equations combine the total drift and diffusion current of electrons and holes. Here, μ_n/μ_p and D_n/D_p are the electron/hole mobility and diffusion coefficient, respectively. Hence, the diode charge transport equations can be written as follows:

$$J = J_n - J_p, \qquad (4)$$

$$J_n = D_n\frac{dn}{dx} + n\mu_n\frac{d\varphi}{dx}, \qquad (5)$$

$$J_p = D_p\frac{dp}{dx} + n\mu_p\frac{d\varphi}{dx}. \qquad (6)$$

(iv) Absorption coefficient equation

The other important parameter is the optical absorption coefficient α(λ), defined as the average penetration depth of a series of photons with the given wavelength λ permeating the semiconductor layers with the bandgap E_g before absorption. The SCAPS-1D software operates various models for estimating the absorption coefficient, which are applied to different semiconducting materials. The mostly addressed optical absorption coefficient model for perovskite solar cells is formulated as follows:

$$\alpha(\lambda) = \left(A + \frac{B}{h\nu} \right) \sqrt{h\nu - E_g} \,, \tag{7}$$

where A and B are the arbitrary constants, h is the Planck constant, ν is the optical frequency of photons, and E_g is the band gap energy of the absorbing layer, respectively.

2.2. Simulation parameters

The semiconducting layer materials and their physical parameters used in the simulations are listed in Table 1. These parameters were carefully selected and have due reference. As the considered materials are disordered semiconductors in nature having defects in their bulk regions, the total photovoltaic response of the device may be hampered by the presence of these defects, especially in the photo-absorbing perovskite layer [20–23]. Therefore, a neutral defect density was introduced into the bulk region of each semiconducting layer. The defect parameters, including the ones of two defect interfaces, ZnO:Al/NaZnBr$_3$ and NaZnBr$_3$/CuI, inserted to induce carrier recombination are presented in Table 2. Finally, all the simulations were carried out by setting the work functions of the front and back contact to 4.4 and 5.1 eV, respectively [24], the room temperature environment (300 K), the standard illumination condition AM 1.5 (1000 W/m^2) and a scanning voltage ranging from 0 to 1.5 V.

3. Results and discussion

3.1. Structure of the simulated PSC and the energy level diagram of the PSC device

The modeled device alongside its energy band structure obtained by simulation is presented in Figs 1a and 1b. The interface offsets of the conduction and valence bands are favorable for flow of charge carriers through the interfaces thus reducing their recombination and quenching losses and resulting in enhanced device performance.

The obtained interface conduction band offset (CBO) and valence band offset (VBO) at the ZnO:Al/NaZnBr$_3$ interface are 0.34 and 1.97 eV, respectively, while the respective values at the NaZnBr$_3$/CuI interface are 1.42 and 0.09 eV, as shown in Fig. 1b.

The value of CBO blocks flow of electrons from the ETM to the perovskite absorbing layer and to the Au back contact for minimal recombination. The large VBO value prevents drift of holes from the Au-back contact to avoid its recombination with electrons in the perovskite absorbing layer. Such CBO and VBO values have an important effect on PSCs as they promote collection of charge carriers, which results in higher photovoltaic performance. The obtained results can form a basis for the studies of PV devices with ZnO:Al, NaZnBr$_3$ and CuI layers.
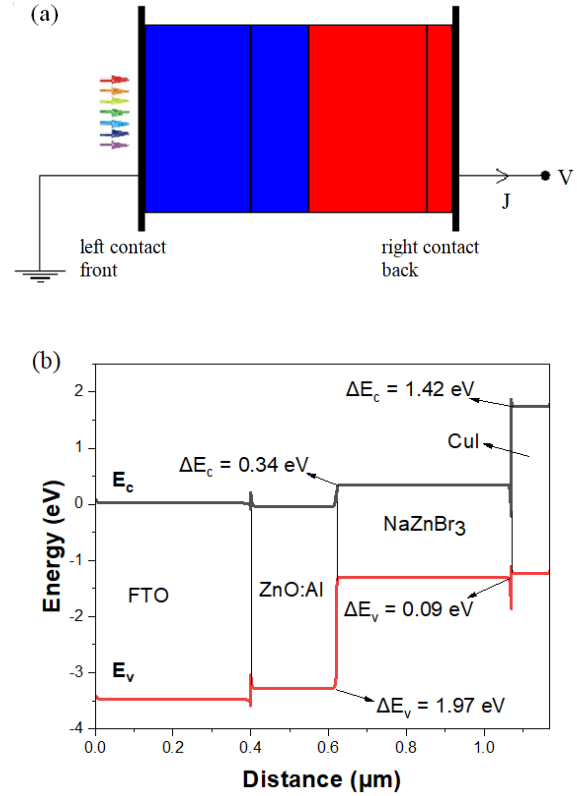

Fig. 1. (a) Structure of the simulated perovskite solar cell and (b) Energy band diagram of a ZnO:Al/NaZnBr$_3$/CuI PSC device.

3.2. Performance study of the initial device

The simulated current density–voltage (J–V) characteristic of the initial device is shown in Fig. 2a. The values of 1.174 V, 14.012 mA/cm^2, 79.649%, and 13.101% were obtained for V_{oc}, J_{sc}, FF, and PCE, respectively. Comparing these solar cell characteristics with the reported experimental values [27], appreciable values of V_{oc} and PCE were obtained which are higher than those from the research work. Such values are expected due to the existence of point defects in the bulk of the absorbing layer as well as recombination centers at the interfaces between the charge transport layers and perovskite absorbing layer [29]. Also, doping the ETM to increase its conductivity and choice of different HTM contributes as well. Fig. 2b shows quantum efficiency (QE) and photon energy (PE) *versus* wavelength. Nonzero QE values correspond to the wavelength range of 300 to 900 nm. This range encompasses the visible spectral region, which satisfies the device requirements. The maximum QE value of 84% is obtained at the wavelength of 360 nm. Strong absorption in the visible region is a determining factor for the light absorption strength. The cut-off value is 750 nm, which corresponds to the band gap of 1.65 eV for NaZnBr$_3$ as shown by the dependence of QE on PE in Fig. 2c.

Table 1. The physical and material parameters for active perovskite layers, a hole-transport layer, and an electron-transport layer are considered in the simulation by SCAPS 1-D.

Parameters	FTO [25]	ZnO:Al [26]	NaZnBr$_3$ [27]	CuI [28]
Thickness (μm)	0.40	0.22	0.45	0.10
Bandgap E_g (eV)	3.50	3.25	1.65	2.98
Electron affinity χ (eV)	4.30	4.00	4.19	2.10
Relative permittivity ε_r	9.00	9.00	5.80	6.50
Effective conduction band density N_c (cm^{-3})	$2.20 \cdot 10^{18}$	$2.00 \cdot 10^{18}$	$1.00 \cdot 10^{16}$	$2.80 \cdot 10^{19}$
Effective valance band density N_v (cm^{-3})	$1.80 \cdot 10^{19}$	$1.80 \cdot 10^{19}$	$1.00 \cdot 10^{16}$	$1.00 \cdot 10^{19}$
Electron thermal velocity (cm/s)	$1.00 \cdot 10^7$	$1.00 \cdot 10^7$	$1.00 \cdot 10^7$	$1.00 \cdot 10^7$
Hole thermal velocity (cm/s)	$1.00 \cdot 10^7$	$1.00 \cdot 10^7$	$1.00 \cdot 10^7$	$1.00 \cdot 10^7$
Electron mobility μ_n (cm²/V·s)	$2.00 \cdot 10^1$	$3.00 \cdot 10^2$	$2.00 \cdot 10^1$	$1.69 \cdot 10^{-4}$
Hole mobility μ_p (cm²/V·s)	$1.00 \cdot 10^1$	$2.50 \cdot 10^1$	$2.00 \cdot 10^1$	$1.69 \cdot 10^{-4}$
Donor concentration N_D (cm^{-3})	$1.00 \cdot 10^{18}$	$7.25 \cdot 10^{18}$	–	–
Acceptor concentration N_A (cm^{-3})	–	–	$1.00 \cdot 10^{19}$	$1.00 \cdot 10^{18}$

Table 2. Defect density values inside the layers and at interface of the device.

Parameters	ETM	HTM	NaZnBr$_3$	NaZnBr$_3$/ETM	HTM/NaZnBr$_3$
Defect type	Neutral	Neutral	Neutral	Neutral	Neutral
Capture cross section electrons (cm^2)	$1.00 \cdot 10^{-15}$	$1.00 \cdot 10^{-15}$	$1.00 \cdot 10^{-15}$	$1.00 \cdot 10^{-15}$	$1.00 \cdot 10^{-18}$
Capture cross section holes (cm^2)	$1.00 \cdot 10^{-15}$	$1.00 \cdot 10^{-15}$	$1.00 \cdot 10^{-15}$	$1.00 \cdot 10^{-15}$	$1.00 \cdot 10^{-16}$
Energetic distribution	Single	Single	Gaussian	Single	Single
Energy level with respect to E_v (above E_v) (eV)	0.6	0.65	0.6	0.60	0.60
Characteristic energy (eV)	0.1	0.1	0.1	0.1	0.1
Total density (integrated over all energies) (1/cm^3)	$1.00 \cdot 10^{15}$	$1.00 \cdot 10^{14}$	$1.00 \cdot 10^{15}$	$1.00 \cdot 10^{11}$	$1.00 \cdot 10^{12}$

3.3. Effect of absorbing layer thickness

The quality and morphology of the absorbing layer play a vital role on the photovoltaic performance of PSCs. In this layer, photogeneration of charge carriers occurs. The performance parameters of PSCs are highly dependent on the absorption layer thickness.

Collection of photoexcited charge carriers is inhibited when the carrier diffusion length is less than the thickness of the absorbing layer. This leads to the increase in the recombination rate of the device and also has a detrimental effect on the device performance [30–32].

In this study, the absorbing layer thickness was varied in the range of 0.1 to 1.3 μm, while the thicknesses of the charge transport layers were fixed. The *J–V* and the QE *versus* wavelength dependences for different absorbing layer thicknesses are shown in Figs. 3a and 3b, respectively. As can be seen from Fig. 3a, J_{sc} increases from 4.950 to 18.188 mA/cm^2, increasing the absorbing layer thickness from 0.1 to 1.3 μm. This increase is attributed to the enhancement of charge carriers photogeneration and distribution within the absorbing layer [33, 34].

Fig. 3b shows the QE *versus* wavelength plots for different thicknesses of the absorbing layer in the wavelength range of 300 to 900 nm. As can be seen from
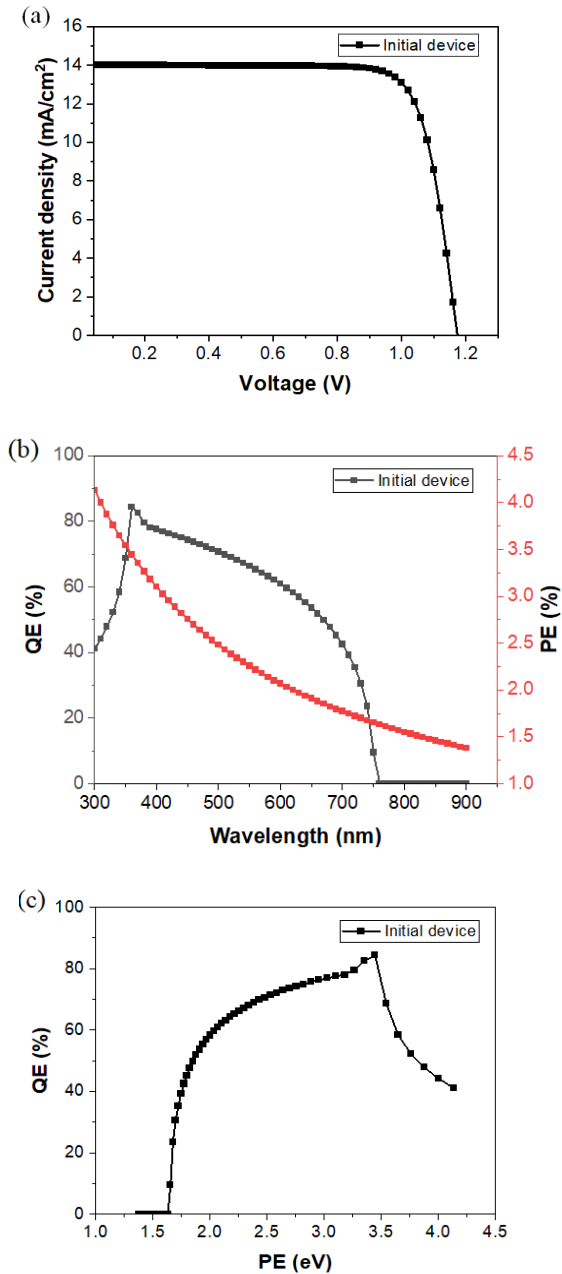
Fig. 2. (a) *J–V* curve of PSC with the initial parameters, (b) quantum efficiency and photon energy of the simulated device *versus* wavelength and (c) quantum efficiency *versus* photon energy.

this figure, QE rapidly increases first with the increment in the absorbing layer thickness from 0.1 to 0.4 μm and reaches steady state at the absorbing layer thicknesses of 0.4 to 1.3 μm. This corresponds to the increment in J_{sc} in Fig. 3a related to the enhancement of photon absorption by the absorbing layer.

The effects of the thickness of absorbing layer on the device photovoltaic parameters FF, PCE and V_{oc}, J_{sc} are shown in Figs 3c and 3d, respectively.

It can be seen from Fig. 3c that FF of the device rapidly increases from 78.828% to 79.610% increasing the absorbing layer thickness from 0.1 to 0.2 μm. A steady increase in the FF value to the maximum for the thicknesses of the absorbing layer between 0.2 to 0.3 μm is observed followed by its steady decrease beyond 0.3 μm. This trend is attributed to resistive losses [31]. The increment of the resistance matches the increase in the absorbing layer thickness, which leads to the corresponding FF decrease [35, 36]. PCE of the device increases sharply from 4.950 to 8.279 mA/cm² increasing the absorbing layer thickness from 0.1 to 0.2 μm. A slight increment in the thickness range of 0.2 to 0.4 μm is observed followed by a steady increase beyond 0.4 μm. This trend is solely due to J_{sc}, while the saturation of PCE is as a result of the saturation of both photo-absorption and J_{sc} [35]. At the thickness of 1.0 μm, the PCE value saturates at 17.215%. The low efficiency at the thicknesses around 0.1-0.2 μm is due to partial light absorption and lower photogeneration. Hence, the optimum PCE value was determined at the absorbing layer thickness of 1.0 μm. Beyond this value, PCE remains quasi-constant.

It can be seen from Fig. 3d that V_{oc} increases with the increase in the thickness of the absorbing layer. This effect is attributed to the absorption of more photons with longer wavelengths [36]. It contributes to generation of excitons as well. In semiconductor theory, V_{oc} can be obtained from Eq. (8), which explains the reliance of V_{oc} on J_{sc} and dark saturation current J_0. It is evident from Eq. (8) that J_0 decreases with the increase in V_{oc}, which can be expressed as follows [37]:

$$V_{oc} = \frac{kT}{q} \ln\left(\frac{J_{sc}}{J_0} + 1\right). \tag{8}$$

Here, k is the Boltzmann constant, T is the temperature, and J_0 is the saturation current density.

It can be seen from the J_{sc} trend that increase in the absorbing layer thickness causes more photons to be absorbed in the device. Therefore, J_{sc} rapidly increases at the initial stage of increasing the absorbing layer thickness from 0.1 to 0.2 μm. A steep rise is observed from 0.2 to 0.3 μm followed by a steady increase. When the layer thickness is over 1 μm and J_{sc} = 18.184 mA/cm², a quasi-constant increment is observed indicating the optimum value. At this, the absorbing layer thickness is sufficient to enable absorption of most of the incident photons as shown in Fig. 3d. The value of J_{sc} may be attributed to the reduction of back-contact recombination current density with the increase of the absorbing layer increases [38]. At ever thicker absorbing layers exceeding the charge carrier diffusion lengths, charge carriers generated close to the perovskite layer center will recombine. A quick and steady increment in J_{sc} observed at this is simply because of the energy gap of the absorbing layer is less than the incident photon energy [39].
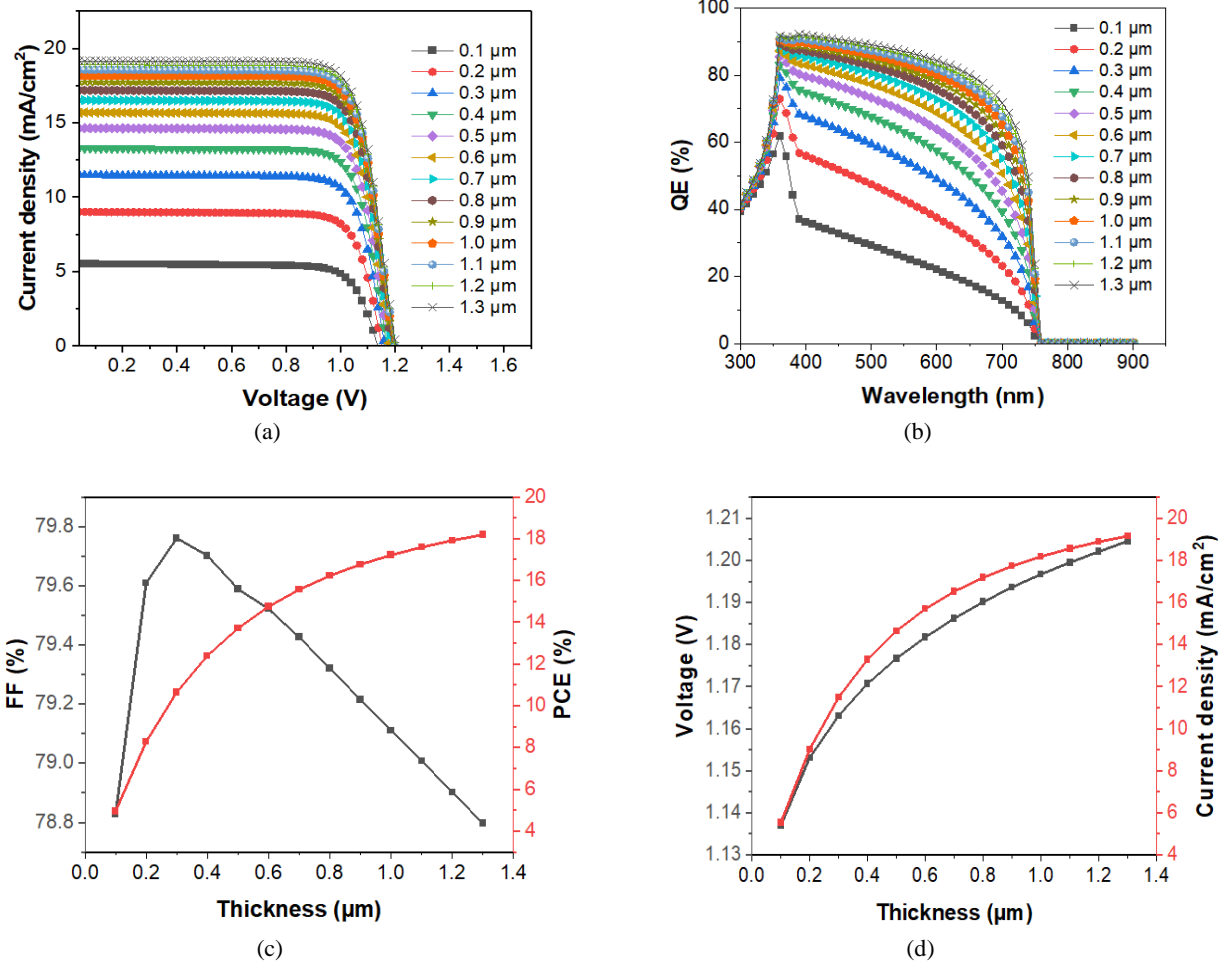
(a)

(b)

(c)

(d)

Fig. 3. (a) *J–V* curves under illumination for different absorbing layer thicknesses, (b) QE *versus* wavelength, (c) FF and PCE *versus* absorbing layer thickness, as well as (d) V_{oc} and J_{sc} *versus* absorbing layer thickness. (Color online.)

3.4. Study of the initial and optimized device performance

The simulated initial and optimized *J–V* characteristics under illumination of the PSC device are shown in Fig. 4. The performance parameters of the optimal device obtained from the simulations are as follows: V_{oc} = 1.197 V, J_{sc} = 18.184 mA·cm^{-2}, FF = 79.110%, and PCE = 17.215%. A 31% increase in PCE and 30% increase in J_{sc} are observed comparing the results for the initial and optimized devices.

3.5. Effect of series resistance on the optimized device

The absorbing layer, the charge transport layers, and the front (FTO) and back (Au) contacts make a significant contribution to the electrical resistance of PSC devices. Simulation for the optimized device was carried out by varying the values of the series resistance from 0 to 10 Ω·cm^2, in order to study its effect on the device performance. Fig. 5a shows *J–V* characteristics at
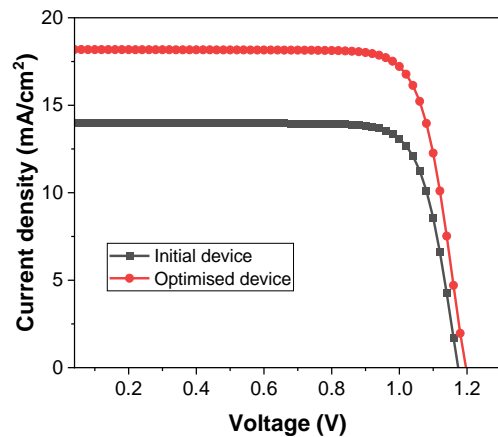

Fig. 4. *J–V* curves for the initial and optimized devices.

different series resistance values, while Figs 5b, 5c present the solar cell parameters *versus* simulated series resistance.
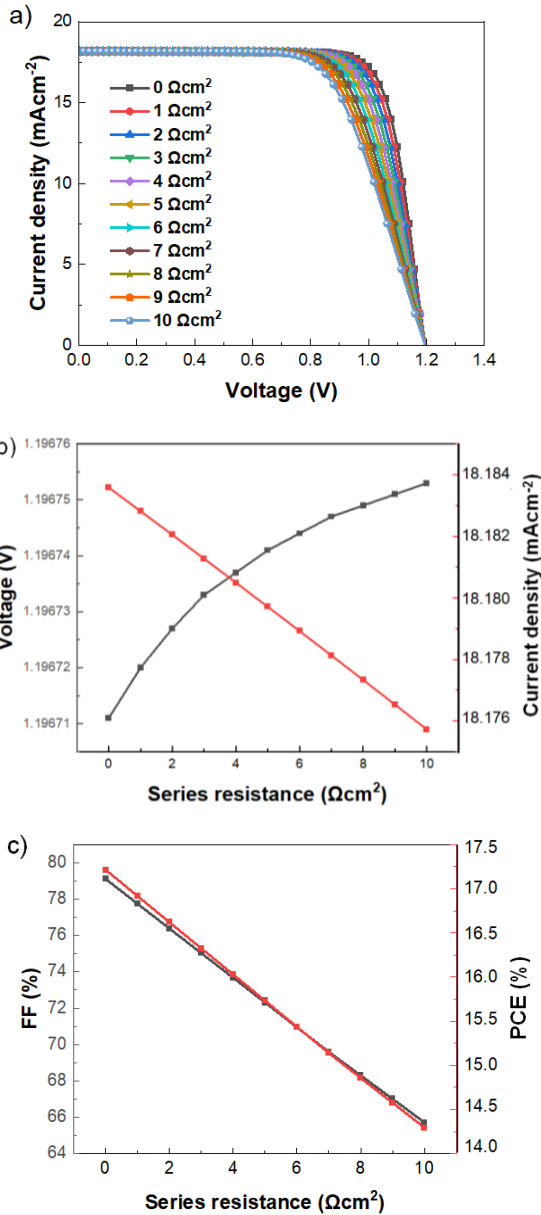
a)

3.6. Effect of shunt resistance on the optimized device

Shunt as well as series resistance cause the main losses in photovoltaic devices, thus providing a relevant analysis of device operation [41]. There are a number of charge recombination pathways responsible for shunt resistance in PSC [42]. The performance of the optimized device was studied by varying the value of the shunt resistance from 10^5 to 10^{30} $\Omega \cdot cm^2$. Fig. 6a shows $J–V$ characteristics for different shunt resistance values, while Figs 6b, 6c present the solar cell parameters *versus* shunt resistance.
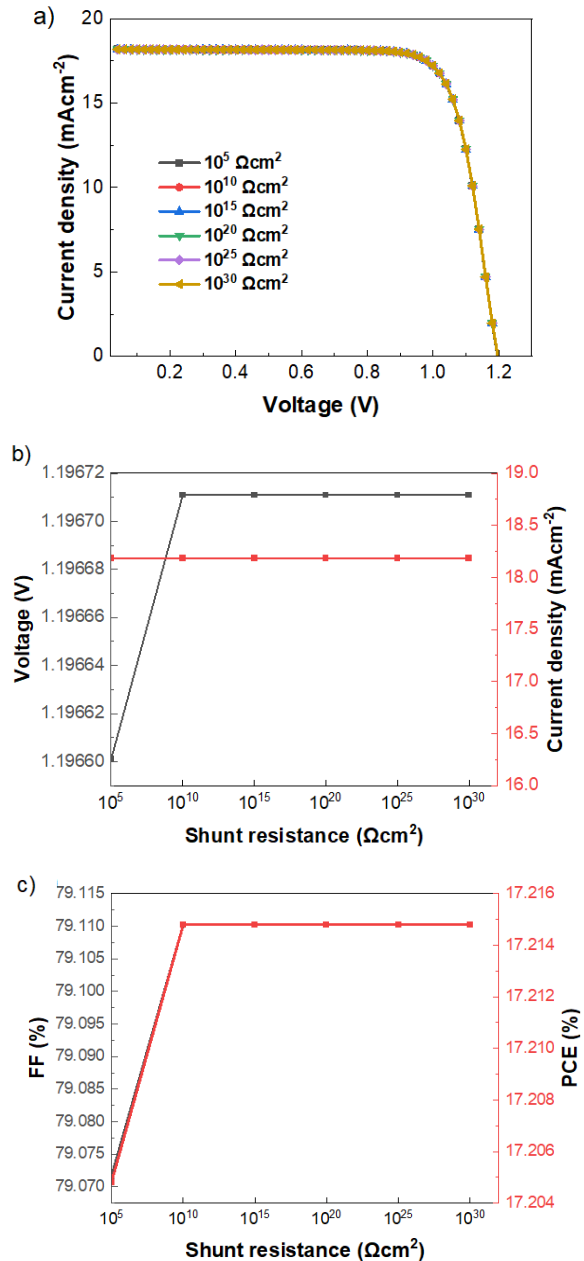
b)

c)

Fig. 5. (a) $J–V$ characteristics under illumination at different series resistance values, (b) V_{oc} and J_{sc}, as well as (c) FF and PCE *versus* series resistance.

a)

b)

c)

Fig. 6. (a) $J–V$ characteristics under illumination at different shunt resistance values, (b) V_{oc} and J_{sc}, as well as (c) FF and PCE *versus* shunt resistance.

As can be seen from Fig. 5b, the device voltage gradually increases when the series resistance grows from 0 to 10 $\Omega \cdot cm^2$. The other photovoltaic parameters such as current density, PCE, and FF are greatly affected at this, as shown in Figs 5b, 5c. The observed decrease in the current density is due to optical transmission losses caused by discoloration [39]. The likely factor conditioning the decrease of the FF with the increase of the series resistance is the transport limitations within the absorbing layer, which results in internal voltage drop [40]. High-efficiency devices have low values of series resistance [41], which is supported by Fig. 5c showing a decrease in the device performance as the series resistance increases.

High values of the shunt resistance lead to improvement of the device efficiency [41], as can be seen from Figs 6b, 6c. In particular, increments in V_{oc} (from 1.1966 to 1.1967 V), FF (from 79.0716% to 79.1102%) and PCE (from 17.2048% to 17.2148%) are observed as the value of the shunt resistance increases from 10^5 to 10^{10} $\Omega \cdot cm^2$ with following saturation of these parameters up to 10^{30} $\Omega \cdot cm^2$. At this, however, J_{sc} does not change with the simulated value of the shunt resistance.
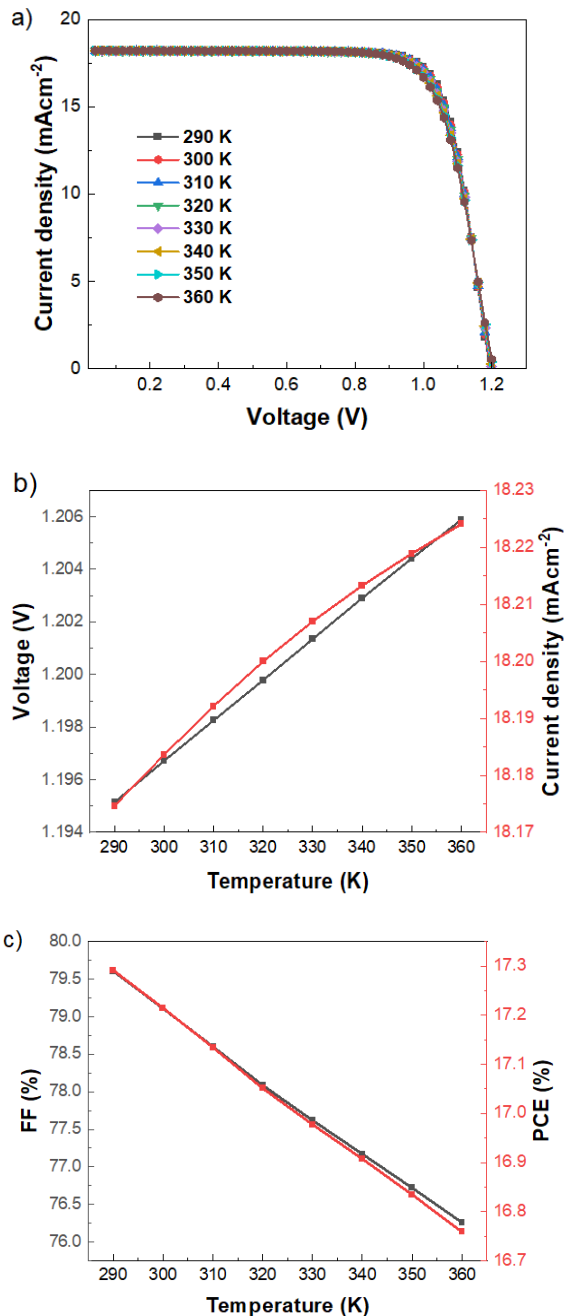

Fig. 7. (a) *J–V* characteristics under illumination at different temperatures, (b) J_{sc} and V_{oc}, as well as (c) PCE and FF *versus* temperature.

3.7. Effect of temperature on the optimized device

Photovoltaic device installations are greatly influenced by the ambient conditions, especially temperature [41]. Generally, PSCs operate at the temperatures exceeding 300 K in outdoor conditions [43]. The photovoltaic properties of the optimized device were explored by simulating the device operation at different temperatures ranging from 290 to 360 K.

Increase of the temperature resulted in a significant reduction in FF and PCE, while increase in the J_{sc} and V_{oc} values was observed. The recombination of electrons and holes is enhanced at high temperatures as the electrons gain more energy before being collected at the electrodes [43].

At extreme temperatures, the band gap, electron and hole mobilities, and carrier concentration in the device become affected. This lowers the device performance [44, 45], as can be seen from Fig. 7c by the decrease in the PCE value. On the other hand, J_{sc} increases, as shown in Fig. 7b, due to the reduction of the band gap and carrier thermal generation rate [46]. The simulated device attains the metastable nature at high temperatures [47].

4. Conclusions

In this study, silver-doped NaZnBr$_3$ perovskite solar cells were numerically investigated using SCAPS-1D simulation software. The effect of the absorbing layer thickness in the range of 0.1 to 1.3 µm on the PSC efficiency was studied. Our study revealed that the optimal photovoltaic parameters were obtained at the absorbing layer thickness of 1.0 µm. For the optimized device (FTO/ZnO:Al/NaZnBr$_3$/CuI/Au), PCE = 17.215%, J_{sc} = 18.184 mA·cm^{-2}, V_{oc} = 1.197 V, and FF = 79.110%. The optimized device had a 31% and 30% upturn in PCE and J_{sc}, respectively, as compared to the initial device. The optimized device was also shown to be affected by series and shunt resistance and temperature. The numerical simulations carried out have paved a way to a better understanding of the way to choose the absorber thickness parameter in order to improve the performance of NaZnBr$_3$ based PSC devices.

References

1. Shaikh S.F., Kwon H.C., Yang W., Mane R.S., Moon J. Performance enhancement of mesoporous TiO$_2$-based perovskite solar cells by ZnS ultrathin-interfacial modification layer. *J. Alloys Compd.* 2018. **738**. P. 405–414. http://dx.doi.org/10.1016/j.jallcom.2017.12.199.

2. Eperon G.E., Burlakov V.M., Docampo P., Goriely A., Snaith H.J. Morphological control for high performance, solution processed planar hetero-junction perovskite solar cells. *Adv. Funct. Mater.* 2014. **24**. P. 151–157. https://doi.org/10.1002/adfm.201302090.

3. Liu M., Johnston M.B., Snaith H.J. Efficient planar heterojunction perovskite solar cells by vapour deposition. *Nature*. 2013. **501**. P. 395–398. https://doi.org/10.1038/nature12509.

4. Min H., Lee D.Y., Kim J. *et al.* Perovskite solar cells with atomically coherent interlayers on SnO$_2$ electrodes. *Nature*. 2021. **598**. P. 444–450. https://doi.org/10.1038/s41586-021-03964-8.

5. Danladi E., Achem C.U., Echi I.O. *et al.* variation study of perovskite layer over the range 100-1300 nm and its influence on the performance of perovskite solar cells using SCAPS software. *J. Nano & Mater. Sci. Res.* 2022. **1**. P. 22–27. https://doi.org/10.20221/jnmsr.v1i.5.

6. Abdulmalik M.O. Performance Optimization of Lead-Free Perovskite Solar Cell with Inorganic Copper Iodide as Hole Transport Material using SCAPS-1D (*Master's dissertation*). Bayero University, Kano, Nigeria, 2019.

7. Sahli F., Werner J., Kamino B.A. *et al.* Fully textured monolithic perovskite/silicon tandem solar cells with 25.2% power conversion efficiency. *Nature Mater.* 2018. **17**, No 9. P. 820–826. http://dx.doi.org/10.1038/s41563-018-0115-4.

8. Zhou D., Zhou T., Tian Y., Zhu X., Tu Y. Perovskite-based solar cells: Materials, methods, and future perspectives. *J. Nanomater.* 2018. **2018**. Art. ID 8148072. 15 p. https://doi.org/10.1155/2018/8148072.

9. Roman-Vazquez M., Vidyasagar C., Munoz-Flores B., Jimenez-Perez V. Recent advances on synthesis and applications of lead- and tin-free perovskites. *J. Alloys Compd.* 2020. **835**. P. 155112. http://dx.doi.org/10.1016/j.jallcom.

10. Sun Y., Gao Y., Hu J. *et al.* Comparison of effects of ZnO and TiO$_2$ compact layer on performance of perovskite solar cells. *J. Solid State Chem.* 2020. **287**. P. 121387. https://doi.org/10.1016/j.jssc.2020.121387.

11. Alias N.S.N.M., Arith F., Mustafa A.N.M. *et al.* Compatibility of Al-doped ZnO electron transport layer with various HTLs and absorbers in perovskite solar cells. *Appl. Opt.* 2022. **61**, No 15. P. 4535–4542. https://doi.org/10.1364/AO.455550.

12. Tseng Z.-L., Chiang C.-H., Chang S.-H., Wu C.-G. Surface engineering of ZnO electron transporting layer *via* Al doping for high efficiency planar perovskite solar cells. *Nano Energy*. 2016. **28**. P. 311–318. https://doi.org/10.1016/j.nanoen.2016.08.035.

13. Bhoomanee C., Ruankham P., Choopun S. *et al.* Effect of Al-doped ZnO for electron transporting layer in planar perovskite solar cells. *Materials Today: Proc.* 2019. **17**, No 4. P. 1259–1267. https://doi.org/10.1016/j.matpr.2019.06.014.

14. Priyanka R., Numeshwar K.S., Sanjay T., Ayush K. Influence of defect density and layer thickness of absorption layer on the performance of tin based perovskite solar cell. *IOP Conf. Series: Mater. Sci. Eng.* 2020. **798**. P. 012020. https://doi.org/10.1088/1757-899X/798/1/012020.

15. Ouslimane T., Et-taya L., Elmaimouni L., Benami A. Impact of absorber layer thickness, defect density, and operating temperature on the performance of MAPbI$_3$ solar cells based on ZnO electron trans-porting material. *Heliyon*. 2021. **7**, No 3. P. e06379. https://doi.org/10.1016/j.heliyon.2021.e06379.

16. Bag A., Radhakrishnan R., Nekovei R., Jeyakumar R. Effect of absorber layer, hole transport layer thickness, and its doping density on the performance of perovskite solar cells by device simulation. *Solar Energy*. 2020. **196**. P. 177–182. https://doi.org/10.1016/j.solener.2019.12.014.

17. Burgelman M., Decock K., Khelifi S., Abass A. Advanced electrical simulation of thin film solar cells. *Thin Solid Film.* 2013. **535**. P. 296–301. https://doi.org/10.1016/j.tsf.2012.10.032.

18. Burgelman M., Verschraegen J., Degrave S., Nollet P. Modeling thin-film PV devices. *Prog. Photovolt.: Res. Appl.* 2004. **12**. P. 143–153. https://doi.org/10.1002/pip.524.

19. Verschraegen J., Burgelman M. Numerical modeling of intra-band tunneling for heterojunction solar cells in scaps. *Thin Solid Film.* 2007. **515**. P. 6276–6279. https://doi.org/10.1016/j.tsf.2006.12.049.

20. Baumann A., Väth S., Rieder P. *et al.* Identification of trap states in perovskite solar cells. *J. Phys. Chem. Lett.* 2015. **6**, No 12. P. 2350–2354. https://doi.org/10.1021/acs.jpclett.5b00953.

21. Rosenfeld D., Schmid P., Széles S. *et al.* Electrical transport properties of thin-film metal-oxide-metal Nb$_2$O$_5$ oxygen sensors. *Sens. Actuators B Chem.* 1996. **37**, issue 1–2. P. 83–89. https://doi.org/10.1016/S0925-4005(96)01991-0.

22. Reza K., Mabrouk S., Qiao Q. A review on tailoring PEDOT:PSS layer for improved performance of perovskite solar cells. *Proc. Nat. Res. Soc.* 2018. **2**. P. 02004. https://doi.org/10.11605/j.pnrs.201802004.

23. Moiz S.A., Alahmadi A.N.M., Karimov Kh.S. Improved organic solar cell by incorporating silver nanoparticles embedded polyaniline as buffer layer. *Solid-State Electron.* 2020. **163**. P. 107658. https://doi.org/10.1016/j.sse.2019.107658.

24. Gan Y., Zhao D., Qin B. *et al.* Numerical simulation of high-performance CsPbI$_3$/FAPbI$_3$ heterojunction perovskite solar cells. *Energies*. 2022. **15**. P. 7301. https://doi.org/10.3390/en15197301.

25. Noh M.F.M., Teh C.H., Daik R. *et al.* The architecture of the electron transport layer for a perovskite solar cell. *J. Mater. Chem. C.* 2018. **6**. P. 682–712. https://doi.org/10.1039/C7TC04649A.

26. Rahman M.M., Khan M.K.R., Islam M.R. *et al.* Effect of Al doping on structural, electrical, optical and photoluminescene properties of nano-structural ZnO thin films. *J. Mater. Sci. Technol.* 2011. **28**, No 4. P. 329–335. https://doi.org/10.1016/S1005-0302(12)60064-4.

27. Emetere M.E., Bello O.O., Afolalu S.A. Enhancement of novel $NaZnBr_3$ perovskite for solar cells application. *Energy Rep.* 2022. **8**. P. 4453–4460. https://doi.org/10.1016/j.egyr.2022.03.087.

28. Hafeez A., Syed Z.H., Mingqing W. A comprehensive device modeling of perovskite solar cell with inorganic copper iodide as hole transport material. *Semicond. Sci. Technol.* 2018. **33**, No 3. P. 035001. https://doi.org/10.1088/1361-6641/aaa596.

29. Islam Md.T., Jani Md.R., Al Amin S.M. *et al.* Numerical simulation studies of a fully inorganic $Cs_2AgBiBr_6$ perovskite solar device. *Opt. Mater.* 2020. **105**. P. 109957. https://doi.org/10.1016/j.optmat.2020.109957.

30. Tan K., Lin P., Wang G. *et al.* Controllable design of solid-state perovskite solar cells by SCAPS device simulation. *Solid-State Electron.* 2016. **126**. P. 75–80. https://doi.org/10.1016/j.sse.2016.09.012.

31. Devi N., Parrey K.A., Aziz A., Datta S. Numerical simulations of perovskite thin-film solar cells using a CdS hole blocking layer. *J. Vac. Sci. Technol. B.* 2018. **36**, No 4. P. 04G105. https://doi.org/10.1116/1.5026163.

32. Liu F., Zhu J., Wei J. *et al.* Numerical simulation: Toward the design of high-efficiency planar perovskite solar cells. *Appl. Phys. Lett.* 2014. **104**. P. 253508. https://doi.org/10.1063/1.4885367.

33. Danladi E., Onimisi M.Y., Garba S. *et al.* Simulation and optimization of lead-based perovskite solar cells with cuprous oxide as a *p*-type inorganic layer. *Journal of the Nigerian Society of Physical Sciences*. 2019. **1**, No 2. P. 72–81. https://doi.org/10.46481/jnsps.2019.13.

34. Danladi E., Dogo D.S., Michael S.U. *et al.* Recent advances in modelling of perovskite solar cells using SCAPS-1D: Effect of absorber and ETM thickness. *East Eur. J. Phys.* 2021. **4**. P. 5–17. https://doi.org/10.26565/2312-4334-2021-4-01.

35. Tchognia J.H.N., Arba Y., Dakhsi K. *et al.* Optimization of the output parameters in kesterite-based solar cells by AMPS-1D. *3rd International Renewable and Sustainable Energy Conference (IRSEC)*, Marrakech, Morocco. 2015. P. 1–6. https://doi.org/10.1109/IRSEC.2015.7454942.

36. Singh P., Ravindra N.M. Temperature dependence of solar cell performance – an analysis. *Sol. Energy Mater. Sol. Cell.* 2012. **101**. P. 36–45. https://doi.org/10.1016/j.solmat.2012.02.019.

37. Khoshsirat N., Yunus N.A.Md., Hamidon M.N., Shafie S., Amin N. Analysis of absorber layer properties effect on CIGS solar cell performance using SCAPS. *Optik.* 2015. **126**. P. 681–686. https://doi.org/10.1016/j.ijleo.2015.02.037.

38. Liu D., Gangishetty M.K., Kelly T.L. Effect of $CH_3NH_3PbI_3$ thickness on device efficiency in planar heterojunction perovskite solar cells. *J. Mater. Chem. A.* 2014. **2**. P. 19873. https://doi.org/10.1039/c4ta02637c.

39. Danladi E., Anselem C.E., Rita C.O. *et al.* Defect and doping concentration study with series and shunt resistance influence on graphene modified perovskite solar cell: A numerical investigation in SCAPS-1D framework. *Journal of the Indian Chemical Society.* 2023. **100**. P. 101001. https://doi.org/10.1016/j.jics.2023.101001.

40. Nandi W., Yiliang W., Daniel W. *et al*. Identifying the cause of voltage and fill factor losses in perovskite solar cells by using luminescence measurements. *Energy Technol.* 2017. **5**. P. 1827–1835. https://doi.org/10.1002/ente.201700374.

41. Karthick S., Velumani S., Bouclé J. Chalcogenide $BaZrS_3$ perovskite solar cells: A numerical simulation and analysis using SCAPS-1D. *Opt. Mater.* 2022. **126**. P. 112250. https://doi.org/10.1016/j.optmat.2022.112250.

42. Pindolia G., Shinde S.M., Jha P.K. Optimization of an inorganic lead free $RbGeI_3$ based perovskite solar cell by SCAPS-1D simulation. *Sol. Energy.* 2022. **236**. P. 802–821. https://doi.org/10.1016/j.solener.2022.03.053.

43. Karimi E., Ghorashi S.M.B. Simulation of perovskite solar cell with P3HT hole-transporting materials. *J. Nanophotonics.* 2017. **11**. P. 032510. http://doi.org/10.1117/1.JNP.11.032510.

44. Nakada T., Mizutani M. 18% efficiency Cd-free $Cu(In, Ga)Se_2$ thin-film solar cells fabricated using chemical bath deposition (CBD)-ZnS buffer layers. *Jpn. J. Appl. Phys.* 2002. **41**. P. L165. http://doi.org/10.1143/JJAP.41.L165.

45. Chelvanathan P., Hossain M.I., Amin N. Performance analysis of copper–indium–gallium–diselenide (CIGS) solar cells with various buffer layers by SCAPS. *Curr. Appl. Phys.* 2010. **10**. P. S387–S391. http://doi.org/10.1016/j.cap.2010.02.018.

46. Ahmed S., Jannat F., Khan Md.A.K., Alim M.A. Numerical development of eco-friendly Cs_2TiBr_6 based perovskite solar cell with all-inorganic charge transport materials via SCAPS-1D. *Optik.* 2021. **225**. P. 165765. https://doi.org/10.1016/j.ijleo.2020.165765.

47. Abdulmalik M.O., Danladi E., Obasi R.C. *et al*. Numerical study of 25.459% alloyed inorganic lead-free perovskite $CsSnGeI_3$-based solar cell by device simulation. *East Eur. J. Phys.* 2022. **4**. P. 125–135. https://doi.org/10.26565/2312-4334-2022-4-12.

Authors and CV

Eli Danladi received his PhD degree from Nigerian Defence Academy in 2020. His research interests are on the fields of materials science, device modeling, nanomaterials and their applications in photovoltaic devices, batteries and supercapacitors.

E-mail: danladielibako@gmail.com,
https://orcid.org/0000-0001-5109-4690

Muhammed Omeiza Abdulmalik received his MSc degree from the Bayero University, Kano in 2019. He is an Assistant Lecturer at the Confluence University of Science and Technology, Osara, Kogi, Nigeria. His research interests include perovskite materials, conducting polymers, materials modeling and application of these materials in photovoltaic devices.
E-mail: abdulmalikmo@custech.edu.ng,
https://orcid.org/0000-0002-3250-7864

Authors' contributions

Muhammed Omeiza Abdulmalik: conceptualization, investigation, data curation, writing – original draft, writing – review & editing, visualization.
Eli Danladi: methodology, validation, data curation, writing – original draft, writing – review & editing.

Вплив товщини перовскіту на ефективність перовскітних сонячних елементів на основі NaZnBr₃, легованого сріблом, досліджений з використанням програмного забезпечення SCAPS

M.O. Abdulmalik, E. Danladi

Анотація. Товщина поглинаючого шару є найважливішим параметром, який істотно впливає на ефективність перовскітних сонячних елементів (ПСЕ). У цій роботі досліджено вплив товщини поглинаючого шару на ефективність перовскітних сонячних елементів на основі $NaZnBr_3$, легованого сріблом, з використанням симулятора ємності одновимірного сонячного елемента SCAPS-1D. Товщину поглинаючого шару варіювали в діапазоні від 100 до 1300 нм. При моделюванні було використано такі початкові значення параметрів сонячного елемента: напруга холостого ходу V_{oc} = 1,174 В, густина струму короткого замикання J_{sc} = 14,012 мА·см$^{-2}$, коефіцієнт заповнення FF = 79,649% та ефективність перетворення потужності PCE = 13,101%. За оптимізованої товщини перовскітного шару, що дорівнювала 1000 нм, було отримано такі значення характеристик сонячного елемента: V_{oc} = 1,197 В, J_{sc} = 18,184 мА·см$^{-2}$, FF = 79,110% та PCE = 17,215%. Значення PCE та J_{sc} збільшились відповідно на 31% та 30% для пристрою з оптимізованими параметрами порівняно з початковим пристроєм. Цей результат підтверджує потенційну можливість відмінного керування фотонами та покращення ефективності перовскітних сонячних елементів шляхом вибору товщини поглинаючого шару.

Ключові слова: SCAPS-1D, перовскітні сонячні елементи, поглинаючий шар, густина струму, ефективність перетворення енергії.